Paratellurite Nanowires as a Versatile Material for THz Phonon Polaritons

Rafael A. Mayer[1,2*], Lukas Wehmeier[3,4,5], Mattheus Torquato[6], Xinzhong Chen[5], Flavio H. Feres[1,2], Francisco C. B. Maia[1], Maximilan Obst[3], Felix G. Kaps[3], Andrei Luferau[3,7], J. Michael Klopf[7], Stephanie N. Gilbert Corder[8], Hans A. Bechtel[8], Juan C. González[9,] Emilson R. Viana[10], Lukas M. Eng[3], Susanne C. Kehr[3], Raul O. Freitas[1], Ingrid D. Barcelos[1*]

1 – Brazilian Synchrotron Light Laboratory (LNLS), Brazilian Center for Research in Energy and Materials (CNPEM), Campinas 13083-970, Brazil
2 – Institute of Physics Gleb Wataghin, State University of Campinas (UNICAMP), Campinas 13083-872, Brazil
3 – Institute of Applied Physics, Technische Universität Dresden, Dresden 01062, Germany
4 – National Synchrotron Light Source II, Brookhaven National Laboratory, Upton, NY 11973, USA
5 – Department of Physics and Astronomy, Stony Brook University, Stony Brook, NY 11790, USA
6 – Material Science and Engineering Section, Instituto Militar de Engenharia (IME), Rio de Janeiro 22290-270, Brazil
7 – Institute of Radiation Physics, Helmholtz-Zentrum Dresden-Rossendorf, Dresden 01328, Germany.
8 – Advanced Light Source (ALS), Lawrence Berkeley National Laboratory, Berkeley, CA 94720, USA
9 – Department of Physics, Universidade Federal de Minas Gerais (UFMG), Belo Horizonte 30123-970, Brazil
10 – Department of Physics, Universidade Tecnológica Federal do Paraná (UTFPR), Curitiba 80230-901, Brazil

Rafael A. Mayer: rafael.mayer@lnls.br
Ingrid D. Barcelos: ingrid.barcelos@lnls.br

Abstract:

Polaritons, i.e. hybrid quasi-particles of light and matter resonances, have been extensively investigated due to their potential to enhance light-matter interactions. Although polaritonic applications thrive in the mid-infrared range, their extension to the terahertz (THz) range remains limited. Here, we present paratellurite (α-TeO_2) nanowires, a versatile material acting as a platform for different types of phonon polaritons. Utilizing synchrotron infrared nanospectroscopy from 10 to 24 THz, we uncover the polaritonic properties of α-TeO_2 nanowires, showcasing their dual

functionality as both a Fabry-Pérot cavity and a waveguide for surface phonon polaritons. Furthermore, near-field measurements with a free-electron laser as a THz source reveal a localized optical contrast down to 5.5 THz, an indication of hyperbolic bands. Our findings complement the repertoire of polaritonic materials, with significant implications for advancing THz technologies.

Keywords: synchrotron, IR nanospectroscopy, one-dimensional materials, tera-hertz, s-SNOM

Introduction

Polaritons, hybrid quasi-particles of light and matter resonances, have garnered significant interest due to their extreme wavelength confinement and ultra-slow group velocities[1,2]. Many applications based on polaritons have flourished in past years, including superlensing[3] photo-detection[4,5], chemical identification[6], and quantum computing[7]. While most of the mentioned applications are in the mid-infrared (mid-IR) window, extending them to far-IR and terahertz (THz) regime remains a formidable challenge[8,9]. THz technology holds immense potential for medical diagnosis[10], security screening[11], food agriculture[12] and pharmaceutics quality[13]. However, photon generation and detection in the so-called 'THz gap' (0.1-10 THz) at room temperature present significant technological hurdles[14]. Moreover, THz characterization techniques at subdiffractional dimensions are still challenging[8,15]. For instance, conventional near-field probes can be inefficient for this spectral range[16,17], while rapid THz detectors are under development. Consequently, the advancement of THz functional materials has been hindered, impeding progress across the entire field.

Recent advancements, fueled by modern quantum cascade lasers, high-brightness light sources and detectors, have accelerated research in THz polaritonics[8,15,17–20]. Within this frequency range, two-dimensional (2D) materials such as semiconductor oxides[21,22], topological insulators[23–25], transition metal dichalcogenides (TMDs)[26] and others[27,28], have demonstrated compelling polariton quality factors and exquisite light confinement. However, their naturally 2D shape allows polariton propagation in all directions, which results in less efficient optical circuitry[29]. The nanopatterning of 2D crystals into IR waveguides has been possible but comes with the compromise of additional fabrication complexity[30]. In contrast, we have recently demonstrated that semiconductor oxides grown as wires can host THz phonon polaritons along its minor axis[31,32]. While THz polariton propagation along the longer axis of these wires is theoretically possible,

there is currently no experimental evidence to support this claim. Table 1 illustrates this issue by comparing different reports of nanostructures across the mid-IR and THz range.

Table 1- Comparison of various experimental reports of nanostructures by their ability to support mid-IR or THz polaritons both as cavity modes across their minor-axis and as guided modes along their longer-axis. Nanostructures that do not require nanopatterning techniques are highlighted in the last column.

1D Nanostructures	Mid-IR		THz (< 600 cm^{-1})		Lithography-free
	(minor axis)	(longer axis)	(minor axis)	(longer axis)	
Carbon nanotubes[33]	✗	✓	✗	✗	✓
hBN nanotubes[34]	✗	✓	✗	✗	✓
hBN nanoribbons[35]	✓	✓	✗	✗	✗
α-MoO_3 nanobelts[31]	✓	✗	✓	✗	✓
SnO_2 nanobelts[32]	✓	✗	✓	✗	✓
α-TeO_2 nanowires	✓	✓	✓	✓	✓

Here, we present nanowires (NWs) of paratellurite (α-TeO_2) as a novel functional platform for THz polaritonics. Paratellurite has already been utilized for THz generation[36], acousto-[37–39], and nonlinear optics[40,41] due to its large refractive index, high-order nonlinear susceptibility, and strong piezo-response. However, this material has not been investigated under the scope of polaritonics. To our knowledge, our work is the first experimental demonstration of THz polariton guiding along the longer axis of a high aspect ratio nanostructure. As shown in Table 1, α-TeO_2 NWs are currently the only material capable of supporting both cavity modes across their minor-axis and quasi-1D guided modes along their longer-axis, spanning from the mid-IR to the THz range. Our work confirms the high crystal quality and the NWs' morphology by employing several characterization techniques, such as X-ray diffraction (XRD), Raman scattering, and electron microscopy. Additionally, by employing scanning near-field optical microscopy (s-SNOM) coupled to a synchrotron light source and a free-electron laser (FEL), we reveal polariton features

across an ultrabroad range from 5.5 to 24 THz. Our results demonstrate the guiding of long-lived (τ~0.6 to 0.9 ps, where τ is the polariton lifetime) surface phonon polaritons (SPhPs) along the NW's longer axis in two bands (around 10.5 and 20 THz). Furthermore, we show spectral near-field patterns along the NW's minor axis, which depend on the SPhPs wavelength, and we explain the results in terms of a Fabry-Perot mechanism. Finally, we exhibit an intense near-field contrast in FEL s-SNOM images at 5.5 THz and 6.5 THz, pointing towards the existence of hyperbolic phonon polariton (HPhPs) inside the challenging 'THz gap'[9]. Hence, our findings underscore the significance of paratellurite NWs in advancing THz polaritonics, inspiring further exploration into the convergence of nanophotonics and other fields.

Material characterization

The α-TeO_2 NWs were synthesized by the reactive thermal evaporation method[42] (see Methods). The composition of the as-synthesized samples was analyzed by energy-dispersive X-ray spectroscopy (EDS), shown in Figure 1a. The EDS was acquired at the center of the wire (red dot in Figure 1b). Only substrate peaks (Si and Cr/Au), Te and O elements are observed. Our samples present well-defined rectangular-like shapes for the morphology of the structure shown by scanning electron microscopy electron (SEM) image in Figure 1b (see Methods). We synthesized NWs of widths (w) varying between 200 and 700 nm, and lengths up to 50 μm. Figure 1c presents the X-ray diffraction (XRD) pattern of the obtained NWs. All the diffraction peaks were indexed to the tetragonal α-TeO_2 crystalline structure (space group P41212, nº. 92) with lattice constants a = b = 4.81 Å and c = 7,61 Å (PDF File # 42-1365)[42,43]. The sharp appearance of the reflection peaks confirms the successful formation of a well-crystallized phase of α-TeO_2, while the absence of non-indexed peaks suggests a single crystalline phase of α-TeO_2 with a [102] preferred growth orientation, as reported by Yan et al. (2014)[44]. These results demonstrate the successful growth of the α-TeO_2 NWs at 400 ºC as proposed. Additionally, Raman measurements of the synthesized NWs confirm the tetragonal (paratellurite, i.e. alpha) crystalline phase of α-TeO_2 with space group $P4_12_12$ (D_4^4) (see supplementary material)[45,46].

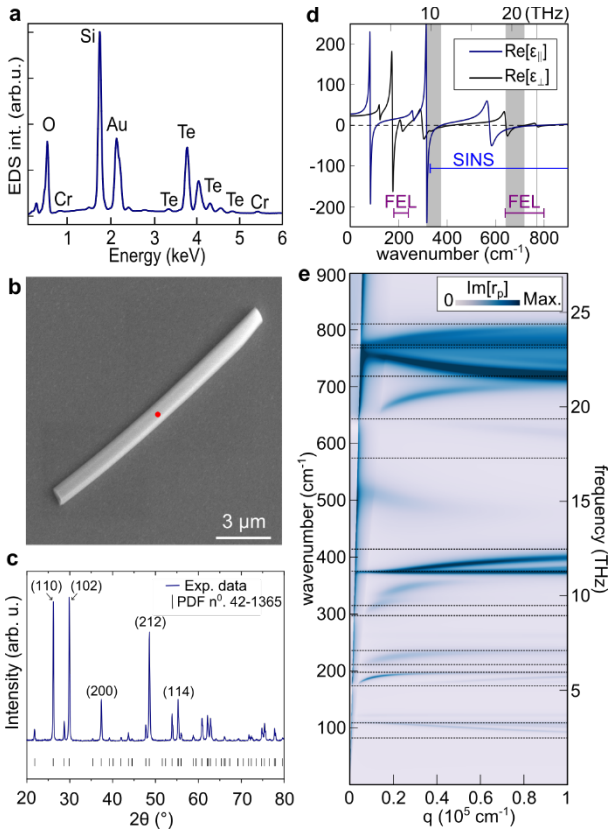

Figure 1 | Overview of α-TeO_2 crystal structure, morphology, and phonon modes. a) EDS measurements acquired in the center of the NW (red dot in Figure 1b) confirm the presence of the constituent elements. **b)** SEM image of α-TeO_2 NWs on the Si/Au substrate. **c)** Corresponding XRD patterns: measurements and phase matching for the α-TeO_2 NWs. **d)** Real part of the in-plane and out-of-plane permittivity of α-TeO_2. The shaded areas represent the SPhP bands studied in this work. The blue and purple intervals indicate the SINS and FEL coverage used in this work. **e)** Calculated dispersion considering an air/α-TeO_2(300 nm)/SiO_2(300nm)/Si layered system. The black dotted lines represent the boundaries between polaritonic bands.

Results

Paratellurite is a uniaxial crystal exhibiting a broad-band phonon activity in the far-IR, ranging from 82 cm^{-1} (2.46 THz) to 811 cm^{-1} (24.31 THz)[47]. Figure 1d displays the real part of the in-plane (⊥) and out-of-plane (∥) components of the dielectric tensor ($\overleftrightarrow{\varepsilon}$). The optical axis of the NWs is oriented perpendicularly to the sample surface. Within this broad range, different flavors of polaritons are supported by α-TeO_2. Elliptical SPhPs (where $Re[\varepsilon_{\parallel}] < 0$ and $Re[\varepsilon_{\perp}] < 0$) can propagate at the interface between α-TeO_2 and materials of positive permittivity ($Re[\varepsilon] > 0$), while HPhPs arise when the components of $Re[\overleftrightarrow{\varepsilon}]$ present opposite signs (For details of the description of $\overleftrightarrow{\varepsilon}$ and the polaritonic bands of α-TeO_2, see supplementary material). Our work

focuses on the SPhP bands (shaded areas in Figure 1d), but THz hyperbolic bands will also be discussed later in the text. Figure 1e reveals the polariton dispersion, calculated through the imaginary part of the Fresnel reflection coefficient ($Im[r_p]$) in p-polarization for a layered air/α-TeO_2 (thickness, $t = 300\ nm$)/SiO_2 (t = 300 nm)/Si system[48]. The dispersion map exhibits two broad SPhP bands at 315 - 376 cm^{-1} and 643 - 720 cm^{-1}, and a narrow SPhP band at 770 – 775 cm^{-1}. The HPhP bands are located at 82 - 109 cm^{-1}, 174 - 198 cm^{-1}, 211 - 236 cm^{-1}, 297 - 315 cm^{-1}, 376 - 414 cm^{-1}, 574 - 643 cm^{-1}, 720 - 770 cm^{-1}, and 775 - 810 cm^{-1}. An additional weak mode outside the α-TeO_2 polariton bands is attributed to the SiO_2 phonon resonance at 458 cm^{-1} [49,50]. Interestingly, due to the hybridization of SPhP at the air/α-TeO_2 and α-TeO_2/SiO_2 boundaries, the dispersion of SPhP is thickness-dependent (see supplementary material). In particular, thinner NWs result in larger confinement, a consequence of the stronger interaction between the surface modes of both interfaces[51]. Moreover, the hybridization of SPhP of both interfaces may be disabled by replacing the substrate with materials of negative permittivity, such as metals (see supplementary material). This completely suppresses the polariton activity in these bands, opening possibilities for applications, such as polariton guiding/cavities induced via substrate engineering[52,53].

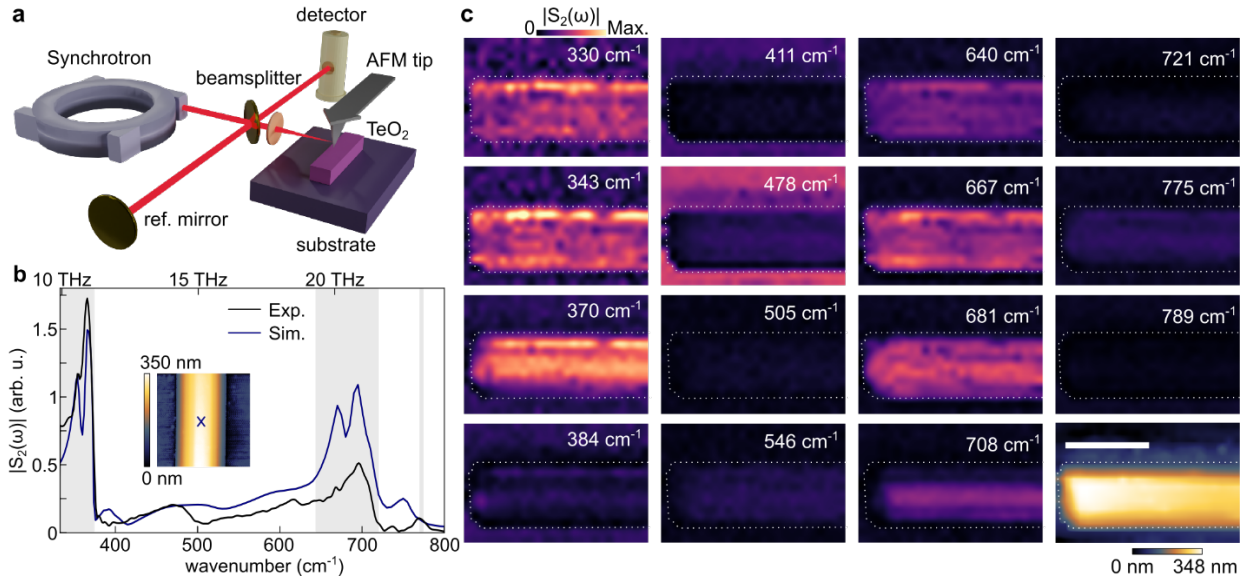

Figure 2 | Synchrotron infrared nano-spectroscopy of paratellurite nanowires - a) Schematics of a SINS experiment. **b)** Simulated and experimental SINS spectra at the center of a α-TeO_2 NW (indicated with a cross in the inset). The shaded area indicates the location of the SPhP bands. The inset shows a 2×2 μm^2 topographic AFM image of the NW. **c)** Hyperspectral images of a α-TeO_2 NW in the same color scale. The bottom right image in the corner shows the AFM topography of

the sample at the same position where the hyperspectral image was taken. The scale bar measures 1 μm. The white dotted lines aid the visualization of the NW boundaries.

To access the far-IR activity of paratellurite NWs, we used synchrotron infrared nano-spectroscopy[54–57] (SINS). As shown in Figure 2a, IR radiation is focused onto the apex of an atomic force microscopy (AFM) tip and confined by the "lightning rod" effect[58]. The scattered radiation from the tip-sample system is then collected by a parabolic mirror and directed to an IR detector. To suppress background scattering, the detected signal is demodulated at the second harmonic of the cantilever's resonance frequency[59,60]. In addition to near-field contrast, SINS enables a full spectral response of the sample by coupling the broadband synchrotron radiation to a s-SNOM apparatus in an asymmetric Michelson interferometer configuration (see Methods for details). Figure 2b shows experimental and simulated point spectra, probed at the center of a NW of width w = 900 nm and thickness t = 350 nm. All simulations in this work were performed using a method detailed in a previous study[61], where a spheroid-shaped tip is positioned above a α-TeO_2 layer on a substrate, matching the experimental sample's dimensions (see the Methods for simulation details).

We observe that the NW enhances the near-field signal predominantly within the SPhP bands, especially within the 315 – 375 cm^{-1} band. Although weak HPhP resonances at 610 cm^{-1} and 740 cm^{-1} are distinguishable in the spectra, they remain considerably weaker than the SPhP resonances. The weak response in the hyperbolic bands cannot be attributed to deviations in the permittivity, as the simulation also predicted the SPhP bands' dominance. Instead, a combination of factors may influence this response, such as: (I) lower values of permittivity on most of the HPhP bands, (II) poor coupling of the tip with the extremely confined HPhPs at 643 - 720 cm^{-1}, and (III) strong overlapping of HPhP branches at the 720 - 770 cm^{-1}, and 775 - 810 cm^{-1} bands. This near-field activity is also reinforced by Figure 2c, where hyperspectral images reveal optical contrast in the bands associated with the SPhP. Even within the narrow SPhP band (approximately 775 cm^{-1}), we observe an enhancement in the near-field amplitude on the NW. Furthermore, we notice a pattern of horizontal stripes on the NW, recognizable in 315 – 375 cm^{-1} and 643 - 720 cm^{-1} SPhP bands. As one may observe, the excitation frequency highly influences spatial dependence on the near-field signal. These near-field patterns, caused by self-interfering SPhPs, will be discussed in the following sections.

Guiding of surface polaritons along the NW's longer-axis

To demonstrate that paratellurite NWs are capable of guiding SPhP waves, we performed SINS spectral linescans on the longer NW's axis (schematic in the inset of Figure 3c). The linescans in Figure 3a reveal fringes whose near-field intensities intrinsically depend on the excitation frequency and the probing position along the NW. The fringe profiles for selected frequencies are presented in Figure 3b, where we observe the polariton wavelength (λ_p) dependence as a function of the excitation frequency (ω). We extracted the polariton momentum by modeling these profiles as SPhP waves launched by the tip and reflected by the NW end. In this model, the SINS amplitude can be described by

$$A(x) = A_0 e^{-2\gamma x} cos(2qx + \varphi) + C_0$$

where $q + i\gamma$ is the complex polariton momentum, φ is an offset phase, C_0 is a background constant, and x is the distance from the initial position of the linescan. We note that our model treats the polaritons as plane waves. While we also considered an alternative model that accounts for circular geometric spread, i.e. $A_0 \propto 1/\sqrt{x}$, the plane wave approximation provided a superior fit to our SINS results. This underscores the quasi-one-dimensional nature of SPhP propagation along the NWs, where the geometric spread is negligible[62].

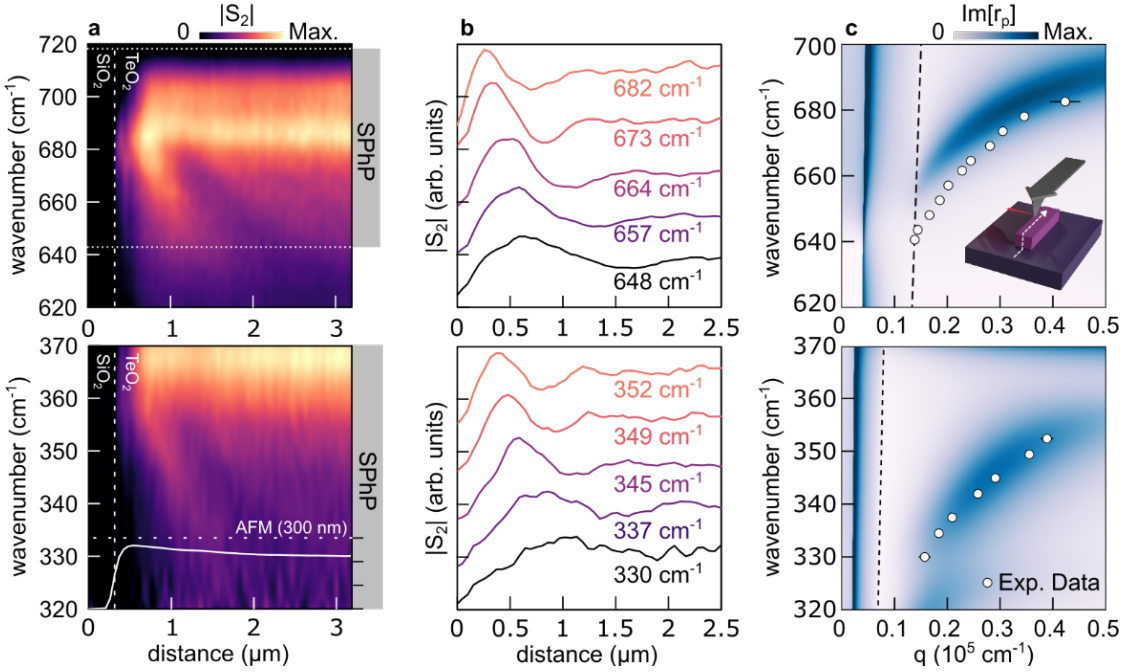

Figure 3 | SINS spectral linescan of guide polaritonic modes along the longer-axis of the α-TeO_2 NWs - a) SINS linescan of a α-TeO_2 NW (t = 240 nm and w = 1150 nm) along its longer axis for the upper SPhP band (top) and lower band (bottom). The white line in the bottom image represents the AFM topography profile. **b)** Near-field profiles for selected frequencies obtained from the linescan in a). **c)** Calculated dispersion of SPhP for an air/α-TeO_2(240 nm)/SiO_2(300 nm)/Si layered system and experimental dispersion extracted from the wave profiles in b) (white circles, the black horizontal lines are uncertainties derived from fitting. Uncertainties bars smaller than the circles are omitted). The dashed black lines are light-lines in a Si environment. Inset in c) illustrates the linescan path.

The comparison between theoretical and experimental dispersions is shown in Figure 3c, yielding reasonable agreement in both SPhP bands. A larger momentum in the experiment for the upper SPhP band may be attributed to a symmetrical surface mode, which may form in such truncated structures[63]. Although these modes are not predicted in the transfer-matrix approach, the $Im[r_p]$ map still provides a good estimate for the guided SPhP dispersion. Furthermore, we notice that the minimum SPhP momentum allowed by the structure is defined by the light-line in the substrate (indicated by the black dashed lines in Figure 3c). For both SPhP bands we calculate the typical figures of merit such as light confinement (λ_0/λ_p), the quality factor $Q = q/\gamma$, the propagation length $L = 1/\gamma$, the group velocity $v_g = d\omega/dq$, and the polariton lifetime $\tau = L/v_g$. The results for specific frequencies are displayed in Table 2 (the corresponding calculations for additional datapoints in both bands are shown in the supplementary materials).

Table 2- Figures of merits of SPhPs in paratellurite. Uncertainties for v_g and τ are not presented here as they were estimated via quadratic interpolation of the real (q) and imaginary part (γ) of the polariton complex momentum (see supplementary material).

Frequency (cm^{-1})	λ_0/λ_p	Q	L (μm)	v_g ($\mu m/s$)	τ (ps)
674	7.2 ± 0.1	4.2 ± 0.4	1.4 ± 0.1	2.1	0.60
350	16.2 ± 0.3	4.0 ± 0.3	1.1 ± 0.7	1.0	0.95

SPhPs in α-TeO_2 are less confined than HPhPs in other polar crystals with THz activity, such as MoO_3, SnO_2, or GeS ($\lambda_0/\lambda_p > 30$)[21,27,32]. Additionally, polaritons in topological insulators present higher confinement ($\lambda_0/\lambda_p > 100$) but suffer from shorter lifetimes (around 0.3 ps)[23,25,64]. This results in similar quality factors ($Q \sim 4$) in comparison to the values reported here. Furthermore, the unique NW shape enables robust guiding of polaritons within a narrow space.

While polaritons in two-dimensional crystals can be guided by reshaping them into waveguides through nanofabrication or by stacking biaxial crystals at specific angles to canalize polaritons[65], these methods have notable limitations. For instance, additional fabrication techniques can deteriorate the structure's walls, affecting the effective polariton lifetime[30]. Moreover, the canalization condition is highly sensitive to the crystals' twisting angle, posing challenges for real nanophotonic applications[66]. α-TeO_2 NWs stand out because they do not require any complex fabrication processes, and their guiding is ensured by the NW's quasi-1D geometry. Hence, they emerge as excellent candidates for THz guiding in the nanoscale.

Cavity of surface polariton modes

Figures 4a and 4b show experimental and simulated SINS linescans of α-TeO_2 NWs, respectively, measured along the minor axis of the NW (inset in Figure 4d) far from its ends. The linescans of both the experiment and simulation present similar near-field features for both bands. At lower frequencies, a near-field enhancement occurs on the edges of the NW (blue rectangle in Figures 4a and 4b). At higher frequencies (red rectangle in Figures 4a and 4b), we observe one near-field peak at the center of the NW that spatially disperses into two peaks. The minor discrepancies in frequency between the simulation and experimental results can be attributed to slight variations in the sample's dielectric function compared to the values found in the literature. To better visualize near-field peaks at higher frequencies, we extract line profiles from the linescans and present them in Figures 4c and 4d. Notably, the single peak at 682 cm^{-1} (355 cm^{-1}, for the lower band) unfolds into two weaker peaks as the frequency increases to 694 cm^{-1} (360 cm^{-1}, respectively).

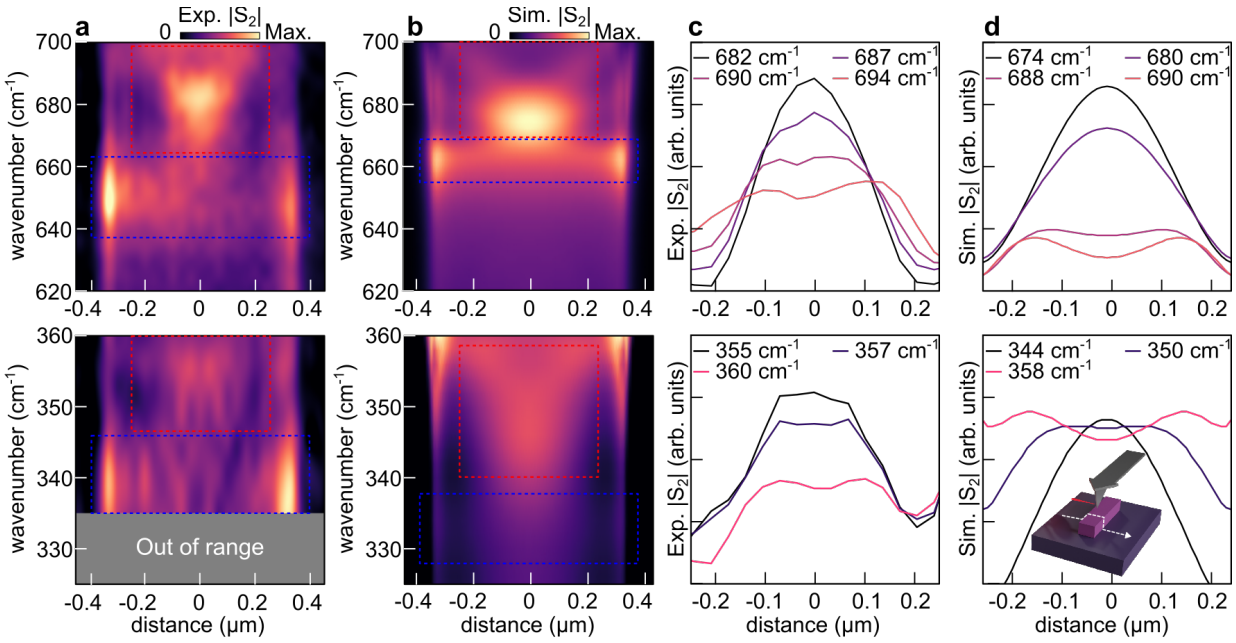

Figure 4 | SINS and simulation of cavity modes of surface polaritons of α-TeO_2 NWs - a) Experimental and **b)** simulated SINS linescans of a NW (t = 115 nm, w = 640 nm) in the transverse direction for upper (top image) and lower (bottom image) SPhP bands. The blue and red rectangles highlight the Fabry-Perot features in the linescans. The grey area represents a spectral band which is out of range of the experiment. **c)** Experimental and **d)** simulated near-field profiles for selected wavenumbers extracted from a) and b), respectively. Inset in d) illustrates the linescan path.

This observed pattern can be understood by modeling the NW as a lossy Fabry-Perot (FP) cavity, wherein SPhPs launched by the tip reflect only a few times on the NW walls before completely decaying. In a low-loss cavity, the modes become resonant at specific frequencies when the polaritons travel multiple times the cavity extension with a round-trip in phase of 2π[67]. However, the short $L/w \sim 2$ ratio results in an interference pattern produced by a maximum of 2 reflections. Thus, only the near-field enhancement for the first and the second FP resonance order may be observed experimentally. The first FP order manifests as a dipolar resonance with hot spots on the sides of the NW (indicated by the blue areas in Figure 4a and 4b), while the central near-field peaks at 355 cm^{-1} and 682 cm^{-1} correspond to a FP resonance of second order. These near-field resonances are blue-shifted in frequency for NWs of smaller width and similar thickness, corroborating with the FP model (see supplementary material for spectral linescans of NWs with different dimensions). The SPhPs become more confined and attenuated at higher frequencies within the bands. Consequently, a single reflection of the SPhPs on the NWs boundaries produces the resulting near-field pattern, leading to the dual peaks observed at 360 cm^{-1} and 694 cm^{-1}.

Nano-spectroscopy in the 'THz gap'

Beyond the spectral range accessible to most synchrotron facilities, the high spectral density of the tunable narrowband FEL allows for s-SNOM studies at very low photon energies down to 40 cm^{-1}. This enabled us to access the THz hyperbolic bands in the α-TeO_2 NWs. Figure 5a contains a schematic of the FEL s-SNOM experiment, where the intense picosecond THz pulses from the FEL illuminate the AFM tip, and the scattered signal is recorded using the self-homodyne technique[20,68]. Similar to the SINS measurements, the far-field contribution to the scattered signal was filtered by higher-harmonics demodulation with a lock-in amplifier at the second harmonic of the cantilever's frequency. While an additional far-field contribution may be present in the detected signal due to the self-homodyne detection, we estimate its variation is negligible within the NW's submicrometric dimensions.

Figure 5b shows near-field images for polaritonic bands in the range from 200 cm^{-1} (6 THz) to 243 cm^{-1} (7.28 THz). These images were taken far from the NW ends. We observe a high contrast inside the NW regions occurring at 220 cm^{-1}. To accurately locate the frequency window of near-field activity, we performed multiple linescans for different FEL frequencies. The result is presented as a spectral linescan in Figure 5c.

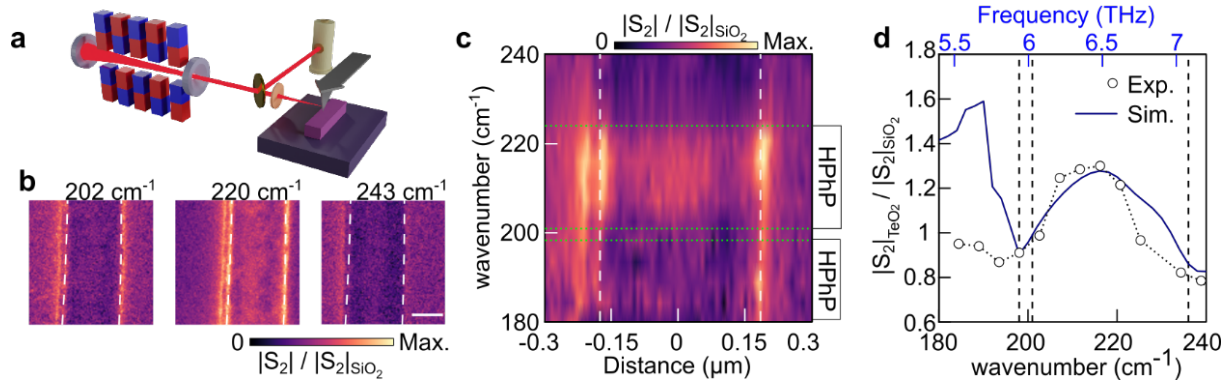

Figure 5 | FEL THz s-SNOM of paratellurite nanowires - a) Schematic of FEL s-SNOM. **b)** Spectral near-field images for selected frequencies. The scale bar corresponds to 200 nm. **c)** FEL spectral linescans on a NW (t = 140 nm, w = 360 nm). The white dashed lines in b) and c) delimit the boundaries of the wire. The dotted green lines indicate the boundaries of the HPhP bands. **d)** The experimental and simulated integrated spectra were obtained from c). The integration path on the x-axis was performed from -0.1 to 0.1 μm.

Despite the lack of a distinct internal structure in the near-field signal on the NW (as in Figure 4a), the spectral linescan allow us to quantify the extent of the THz active bands in α-TeO_2.

To better elucidate this, we integrated the linescan along the spatial coordinate inside the NW region. The result of this integration is displayed in Figure 5d, along with a simulation of the near-field spectral response of the wire. We demonstrate the validity of this method by comparing the results with simulated and SINS point spectra at the 620 – 720 cm^{-1} SPhP band (see supplementary material). The experiment and the simulation align well, indicating the presence of two resonances: one at 190 cm^{-1} and another at 215 cm^{-1}. The peak positions completely agree with the emergence of two hyperbolic regions at these longer wavelengths. We hypothesize that despite the narrow bandwidth of FEL radiation[21], the small splitting between longitudinal and transverse optical phonons, along with the highly dispersive nature of HPhP in these bands, prevented us from resolving the polariton fringes. However, the enhanced near-field signal in these bands points towards the existence of highly confined HPhPs in paratellurite NWs.

Conclusion

Overall, our study introduces paratellurite NWs as platform for THz polaritonics. Empowered by large light source facilities such as the Synchrotron light source and the FEL, we have demonstrated through near-field microscopy the capability of α-TeO_2 NWs to efficiently guide SPhPs with competitive lifetimes ($\tau \sim 0.9$ ps) at the far-IR frequencies. Notably, the inherently straightforward integration of the as-synthesized NWs as waveguides into nanophotonic devices offers a distinct advantage over two-dimensional materials, eliminating the need for additional nanopatterning steps.

Moreover, we revealed intense near-field hot-spots along the NW cross-section, elucidated through a simple Fabry-Perot model. These hot-spots may be harvested in the future to enhance light-matter interactions at wavelengths traditionally challenging to be probed. Additionally, we indicate the existence of hyperbolic polaritons by revealing their spectral signatures inside the "THz gap". Further studies can delve deeper into the THz hyperbolic polaritons in α-TeO_2 as the THz infrastructure for s-SNOM continues to develop.

Our study is the first to experimentally demonstrate that high-aspect-ratio nanostructures can serve multiple purposes, functioning as both a cavity and a waveguide in the mid-IR and THz ranges (see Table 1 for a comparison with other works). The broadband phononic activity of α-TeO_2 enables applications in nano-optical communication by offering several polaritonic bands, i.e. channels, for data transmission. Moreover, α-TeO_2 nanowires show potential for remote bio-

sensing, as they allow for polariton coupling with a wide range of resonances, from mid-IR vibrational resonances of organic molecules to THz rotational transitions of greenhouse gases [6,69,70]. Finally, it is important to acknowledge the exceptional third-order nonlinear susceptibility and piezoelectric response inherent to paratellurite. Exciting applications may emerge by harnessing these distinctive properties in α-TeO_2-based nanophotonic devices. For example, enhancing near-field interaction could significantly improve second-harmonic generation efficiency[71]. Exploring surface acoustic waves in nanophotonics also presents another promising avenue for leveraging these properties[61]. Thus, our findings highlight the potential of paratellurite NWs in advancing THz polaritonics, inspiring further exploration to merge nano-, non-linear, and acousto-optics.

Methods

Sample fabrication

The synthesis of α-TeO_2 nanowires was performed based on the paper Jpn. J. Appl. Phys. 47, 771, 2008. A ceramic crucible was used, where small pieces of high-purity metallic Te were placed. On top of the crucible, a Si substrate was positioned as a lid. The crucible was placed in a Lindberg-Blue M Thermo Scientific furnace, and the system was heated to 400 °C (at a rate of 20 °C/min) *in* the presence of a small flow of oxygen, around 100 sccm. After 2 hours at 400 °C, the furnace was turned off and cooled naturally until room temperature[42]. As a result of this process, a layer of the white product was deposited on the undersurface of the wafer.

SEM and EDS

The scanning electron microscopy (SEM) and the energy-dispersive x-ray spectroscopy (EDS) measurements were carried out in a Thermo Scientific Helios 5 PFIB CXe DualBeam.

XRD

The phase and the crystal structure were analyzed by X-ray diffraction (XRD). The XRD pattern was obtained using a Rigaku/Geirgeflex diffractometer at room temperature with Cu-Kα radiation (λ = 1.5408 Å).

Raman

The Raman spectroscopy measurement was performed at 532 nm laser excitation in a Witec® Alpha300 RA spectrometer. The data were treated by a deconvolution of the bands using Lorentzian curves to fit (see supplementary material for vibrational modes assignment).

Synchrotron infrared nano-spectroscopy

SINS experiments were performed at the Advanced Light Source (ALS) at the Lawrence Berkeley National Lab (LBNL). The SINS technique combines a high-brightness, broadband synchrotron light source (frequency window is 330-4000 cm^{-1}), with a FTIR spectrometer and an AFM probe[57,72]. The beamline optical setup consists of an asymmetric Michelson interferometer mounted into a commercial s-SNOM microscope (NeaSNOM, Neaspec GmBH), which can be described as an AFM with suitable optical access to excite and collect the near-field scattered light. In the interferometer, the incident synchrotron IR beam is split in two components by a KRS-5 beamsplitter defining the two interferometer arms, consisting of a metal-coated AFM tip (tip arm) and an IR high-reflectivity mirror mounted onto a translation stage (scanning arm). The IR beam component of the tip arm is focused by a parabolic mirror on the tip-sample region. In the experiment, the AFM operates in semi-contact (tapping) mode, wherein the tip is electronically driven to oscillate in its fundamental mechanical frequency Ω (~250 kHz) near the sample surface. The incident light interacts with the metal coated tip and sample, creating an effective local polarization. The back-scattered light stemming from this tip-sample interaction, composed of far- and near-field contributions, is collected by a high-speed IR detector and a lock-in amplifier having Ω as the reference frequency. The clean optical near-field (S_n), originated from a sample area of radius comparable to the tip radius (around 25 nm in our case), is given by the back-scattered light components modulated in higher harmonics (n) of Ω, with $n \geq 2$. Displacing the mirror in the scanning arm in this asymmetric scheme creates complex interferograms that can be Fourier-transformed to yield amplitude $|S_n(\omega)|$ and phase $\Phi_n(\omega)$ spectra. All SINS spectra here are given by n = 2, i.e., $S_2(\omega)$. For the Far-IR measurements at ALS Beamline 2.4, a customized Ge:Cu photoconductor, which provides broadband spectral detection down to 320 cm^{-1}, and a KRS-5 beamsplitter were employed. Therein, we obtain 20 SINS spectra per point in our measurements, which are averaged and normalized to a reference spectrum obtained from a pure gold surface.

Free-electron laser s-SNOM

FEL-s-SNOM near-field images were measured at the free-electron laser FELBE at the Helmholtz-Zentrum Dresden-Rossendorf (HZDR, Dresden, Germany). The pulsed (13 MHz) radiation generated from FELBE can be tuned from 40 to 2000 cm^{-1} with a spectral width of ~1% of the central wavenumber. We utilized a Pt–Ir-coated Si tip for the s-SNOM experiment and collected

the radiation with a MCT and a Ge:Ga photoconductive detector for lower frequencies (<300cm^{-1})[20]. Details of data treatment can be found in supplemental materials.

Near-field simulations

The hyperspectral images depicted in Figure 4 were generated through numerical simulations employing a previously demonstrated method[61]. In this approach, the probe tip is represented as an elongated spheroid with a length of 600 nm and an apex radius of curvature of 30 nm, positioned above a layered sample comprising a α-TeO_2 film on a substrate. The dimensions of the α-TeO_2 layer—900 nm in width and 350 nm in thickness—mirror those of the actual sample utilized in the experiments. The simulation of the electromagnetic interaction between the tip and the sample is conducted using the frequency-domain finite-element method (FEM) solver COMSOL Multiphysics. This involves calculating the tip's dipole moment at various distances from the sample, with the assumption of a tapping amplitude of 50 nm. The dipole moment, which influences the far-field scattering, is subsequently demodulated at the second harmonic of the tip's oscillation frequency to estimate the near-field signal S_2. Simulations were carried out to construct the hyperspectral images across a range of lateral tip positions and excitation frequencies. To enhance computational efficiency, a 2D model was chosen over a 3D one, though it is noted that the outcomes from 3D simulations are qualitatively congruent with those obtained from 2D simulations. In a previous study[73], the same 2D approximation was used, and it also demonstrated excellent consistency with experimental results.

Supporting Information

Section 1 (S1): Raman of paratellurite
Section 2 (S2): Dielectric function of paratellurite and polariton bands
Section 3 (S3): Thickness-dependent dispersion of SPhPs
Section 4 (S4): Figures of merit of SPhPs
Section 5 (S5): Comparison of cavity resonances for other NW dimensions
Section 6 (S6): FEL s-SNOM data processing
Section 7 (S7): Simulation of hyperbolic and surface modes

Acknowledgments

We thank Prof. Mengkun Liu and his team for the insightful discussion, Prof. Geraldo Mathias Ribeiro for the synthesis of the nanostructures, and Prof. Daniel Bretas Roas and the Center of Microscopy at the Universidade Federal de Minas Gerais (CM-UFMG) for the electron

microscopy measurements and TEM sample preparation. This work was supported by Fundação de Amparo à Pesquisa do Estado de São Paulo (FAPESP) Young Investigator Grant 2019/14017-9 and grant 2020/15740-3. The authors acknowledge financial support from Conselho Nacional de Desenvolvimento Científico e Tecnológico (CNPq) under grant nos. 406139/2018-0, 305808/2018-4, 306170/2023-0, 309946/2021-2 and 302632/2022-0. The authors acknowledge the financial support of CAPES, Fundação de Amparo à Pesquisa do Estado de Minas Gerais (FAPEMIG) under the grant APQ-03044-17. I.D.B. acknowledges the financial support from the Brazilian Nanocarbon Institute of Science and Technology (INCT/Nanocarbono). All authors would like to acknowledge the facilities Brazilian Synchrotron Light Laboratory (LNLS), Advanced Light Source (ALS) and the Free-Electron Laser (FELBE) in Dresden for support in nano-optics experiments. L.W. acknowledges funding by the U.S. Department of Energy, Office of Science, National Quantum Information Science Research Centers, Co-design Center for Quantum Advantage (C2QA) under contract number DE-SC0012704. This research used resources of the Advanced Light Source, which is a DOE Office of Science User Facility under contract no. DE-AC02-05CH11231. Also, we thank the Laboratory of Microscopy Samples (LAM) for sample preparation and characterization Proposal No.: 2022151 at LNLS/CNPEM. The TU Dresden team (L.W., M.O., F.G.K., L.M.E., S.C.K.) acknowledges funding by the Bundesministerium für Bildung und Forschung (BMBF, Federal Ministry of Education and Research, Germany, Project Grant Nos., 05K16ODA and 05K19ODB) as well as by the Deutsche Forschungsgemeinschaft (DFG, German Research Foundation) under Germany's Excellence Strategy through the *Würzburg-Dresden Cluster of Excellence on Complexity and Topology in Quantum Matter* – ct.qmat (EXC 2147, project-id 390858490) and through the Collaborative Research Center on *Chemistry of Synthetic Two-Dimensional Materials* – CRC1415 (ID: 417590517).

Funding Sources

This work was supported by Fundação de Amparo à Pesquisa do Estado de São Paulo (FAPESP) Young Investigator Grant 2019/14017-9 and grant 2020/15740-3; Conselho Nacional de Desenvolvimento Científico e Tecnológico (CNPq) under grant nos. 406139/2018-0, 305808/2018-4, 306170/2023-0, 309946/2021-2 and 302632/2022-0; CAPES; Fundação de Amparo à Pesquisa do Estado de Minas Gerais (FAPEMIG) under the grant APQ-03044-17; U.S. Department of Energy, Office of Science, National Quantum Information Science Research Centers, Co-design Center for Quantum Advantage (C2QA) under contract number DE-SC0012704; Advanced Light Source, which is a DOE Office of Science User Facility under contract no. DE-AC02-05CH11231; Bundesministerium für Bildung und Forschung (BMBF, Federal Ministry of Education and Research, Germany, Project Grant Nos., 05K16ODA and 05K19ODB); Deutsche Forschungsgemeinschaft (DFG, German Research Foundation) under Germany's Excellence Strategy through the *Würzburg-Dresden Cluster of Excellence on Complexity and Topology in Quantum Matter* – ct.qmat (EXC 2147, project-id 390858490) and

the Collaborative Research Center on *Chemistry of Synthetic Two-Dimensional Materials* – CRC1415 (ID: 417590517).

References

(1) Basov, D. N.; Fogler, M. M.; García de Abajo, F. J. Polaritons in van Der Waals Materials. *Science (1979)* **2016**, *354* (6309), aag1992. https://doi.org/10.1126/science.aag1992.

(2) Yoxall, E.; Schnell, M.; Nikitin, A. Y.; Txoperena, O.; Woessner, A.; Lundeberg, M. B.; Casanova, F.; Hueso, L. E.; Koppens, F. H. L.; Hillenbrand, R. Direct Observation of Ultraslow Hyperbolic Polariton Propagation with Negative Phase Velocity. *Nat Photonics* **2015**, *9* (10), 674–678. https://doi.org/10.1038/nphoton.2015.166.

(3) Li, P.; Lewin, M.; Kretinin, A. V.; Caldwell, J. D.; Novoselov, K. S.; Taniguchi, T.; Watanabe, K.; Gaussmann, F.; Taubner, T. Hyperbolic Phonon-Polaritons in Boron Nitride for near-Field Optical Imaging and Focusing. *Nat Commun* **2015**, *6* (1), 7507. https://doi.org/10.1038/ncomms8507.

(4) Castilla, S.; Vangelidis, I.; Pusapati, V.-V.; Goldstein, J.; Autore, M.; Slipchenko, T.; Rajendran, K.; Kim, S.; Watanabe, K.; Taniguchi, T.; Martín-Moreno, L.; Englund, D.; Tielrooij, K.-J.; Hillenbrand, R.; Lidorikis, E.; Koppens, F. H. L. Plasmonic Antenna Coupling to Hyperbolic Phonon-Polaritons for Sensitive and Fast Mid-Infrared Photodetection with Graphene. **2020**, *11* (4872), 1–9.

(5) Wu, C.; Ku, C.; Yu, M.; Yang, J.; Wu, P.; Huang, C.; Lu, T.; Huang, J.; Ishii, S.; Chen, K. Near-Field Photodetection in Direction Tunable Surface Plasmon Polaritons Waveguides Embedded with Graphene. *Advanced Science* **2023**, *10* (30), 1–7. https://doi.org/10.1002/advs.202302707.

(6) Dolado, I.; Maciel-Escudero, C.; Nikulina, E.; Modin, E.; Calavalle, F.; Chen, S.; Bylinkin, A.; Alfaro-Mozaz, F. J.; Li, J.; Edgar, J. H.; Casanova, F.; Vélez, S.; Hueso, L. E.; Esteban, R.; Aizpurua, J.; Hillenbrand, R. Remote Near-Field Spectroscopy of Vibrational Strong Coupling between Organic Molecules and Phononic Nanoresonators. *Nat Commun* **2022**, *13* (1), 6850. https://doi.org/10.1038/s41467-022-34393-4.

(7) Alonso Calafell, I.; Cox, J. D.; Radonjić, M.; Saavedra, J. R. M.; García de Abajo, F. J.; Rozema, L. A.; Walther, P. Quantum Computing with Graphene Plasmons. *npj Quantum Inf* **2019**, *5* (1), 37. https://doi.org/10.1038/s41534-019-0150-2.

(8) Guo, X.; Bertling, K.; Donose, B. C.; Brünig, M.; Cernescu, A.; Govyadinov, A. A.; Rakić, A. D. Terahertz Nanoscopy: Advances, Challenges, and the Road Ahead. *Appl Phys Rev* **2024**, *11* (2), 21306. https://doi.org/10.1063/5.0189061.

(9) Borak, A. Toward Bridging the Terahertz Gap with Silicon-Based Lasers. *Science (1979)* **2005**, *308* (5722), 638–639. https://doi.org/10.1126/science.1109831.

(10) Zaytsev, K. I.; Dolganova, I. N.; Chernomyrdin, N. V; Katyba, G. M.; Gavdush, A. A.; Cherkasova, O. P.; Komandin, G. A.; Shchedrina, M. A.; Khodan, A. N.; Ponomarev, D. S.; Reshetov, I. V; Karasik, V. E.; Skorobogatiy, M.; Kurlov, V. N.; Tuchin, V. V. The Progress and Perspectives of Terahertz Technology for Diagnosis of Neoplasms: A Review. *Journal of Optics* **2019**, *22* (1), 13001. https://doi.org/10.1088/2040-8986/ab4dc3.

(11) Tzydynzhapov, G.; Gusikhin, P.; Muravev, V.; Dremin, A.; Nefyodov, Y.; Kukushkin, I. New Real-Time Sub-Terahertz Security Body Scanner. *J Infrared Millim Terahertz Waves* **2020**, *41* (6), 632–641. https://doi.org/10.1007/s10762-020-00683-5.

(12) Afsah-Hejri, L.; Akbari, E.; Toudeshki, A.; Homayouni, T.; Alizadeh, A.; Ehsani, R. Terahertz Spectroscopy and Imaging: A Review on Agricultural Applications. *Comput Electron Agric* **2020**, *177*, 105628. https://doi.org/10.1016/j.compag.2020.105628.

(13) Zeitler, J. A.; Taday, P. F.; Newnham, D. A.; Pepper, M.; Gordon, K. C.; Rades, T. Terahertz Pulsed Spectroscopy and Imaging in the Pharmaceutical Setting - a Review. *Journal of Pharmacy and Pharmacology* **2007**, *59* (2), 209–223. https://doi.org/10.1211/jpp.59.2.0008.

(14) Rizza, C.; Molle, A. Closing the THz Gap with Dirac Semimetals. *Light Sci Appl* **2022**, *11* (1), 124. https://doi.org/10.1038/s41377-022-00812-w.

(15) Cocker, T. L.; Jelic, V.; Hillenbrand, R.; Hegmann, F. A. Nanoscale Terahertz Scanning Probe Microscopy. *Nat Photonics* **2021**, *15* (8), 558–569. https://doi.org/10.1038/s41566-021-00835-6.

(16) Mastel, S.; Lundeberg, M. B.; Alonso-González, P.; Gao, Y.; Watanabe, K.; Taniguchi, T.; Hone, J.; Koppens, F. H. L.; Nikitin, A. Y.; Hillenbrand, R. Terahertz Nanofocusing with Cantilevered Terahertz-Resonant Antenna Tips. *Nano Lett* **2017**, *17* (11), 6526–6533. https://doi.org/10.1021/acs.nanolett.7b01924.

(17) Bosco, L.; Franckié, M.; Scalari, G.; Beck, M.; Wacker, A.; Faist, J. Thermoelectrically Cooled THz Quantum Cascade Laser Operating up to 210 K. *Appl Phys Lett* **2019**, *115* (1), 10601. https://doi.org/10.1063/1.5110305.

(18) Wehmeier, L.; Liu, M.; Park, S.; Jang, H.; Basov, D. N.; Homes, C. C.; Carr, G. L. Ultrabroadband Terahertz Near-Field Nanospectroscopy with a HgCdTe Detector. *ACS Photonics* **2023**, *10* (12), 4329–4339. https://doi.org/10.1021/acsphotonics.3c01148.

(19) Chen, X.; Hu, D.; Mescall, R.; You, G.; Basov, D. N.; Dai, Q.; Liu, M. Modern Scattering-Type Scanning Near-Field Optical Microscopy for Advanced Material Research. *Advanced Materials* **2019**, *31* (24), 1–24. https://doi.org/10.1002/adma.201804774.

(20) Kuschewski, F.; von Ribbeck, H.-G.; Döring, J.; Winnerl, S.; Eng, L. M.; Kehr, S. C. Narrow-Band near-Field Nanoscopy in the Spectral Range from 1.3 to 8.5 THz. *Appl Phys Lett* **2016**, *108* (11), 113102. https://doi.org/10.1063/1.4943793.

(21) de Oliveira, T. V. A. G.; Nörenberg, T.; Álvarez-Pérez, G.; Wehmeier, L.; Taboada-Gutiérrez, J.; Obst, M.; Hempel, F.; Lee, E. J. H.; Klopf, J. M.; Errea, I.; Nikitin, A. Y.; Kehr, S. C.; Alonso-González, P.; Eng, L. M. Nanoscale-Confined Terahertz Polaritons in a van Der Waals Crystal. *Advanced Materials* **2021**, *33* (2), 2005777. https://doi.org/10.1002/adma.202005777.

(22) Sun, T.; Chen, R.; Ma, W.; Wang, H.; Yan, Q.; Luo, J.; Zhao, S.; Zhang, X.; Li, P. Van Der Waals Quaternary Oxides for Tunable Low-Loss Anisotropic Polaritonics. *Nat Nanotechnol* **2024**, *19* (6), 758–765. https://doi.org/10.1038/s41565-024-01628-y.

(23) Chen, S.; Leng, P. L.; Konečná, A.; Modin, E.; Gutierrez-Amigo, M.; Vicentini, E.; Martín-García, B.; Barra-Burillo, M.; Niehues, I.; Maciel Escudero, C.; Xie, X. Y.; Hueso, L. E.; Artacho, E.; Aizpurua, J.; Errea, I.; Vergniory, M. G.; Chuvilin, A.; Xiu, F. X.; Hillenbrand, R. Real-Space Observation of Ultraconfined in-Plane Anisotropic Acoustic Terahertz Plasmon Polaritons. *Nat Mater* **2023**, *22* (7), 860–866. https://doi.org/10.1038/s41563-023-01547-8.

(24) Chen, S.; Bylinkin, A.; Wang, Z.; Schnell, M.; Chandan, G.; Li, P.; Nikitin, A. Y.; Law, S.; Hillenbrand, R. Real-Space Nanoimaging of THz Polaritons in the Topological Insulator Bi2Se3. *Nat Commun* **2022**, *13* (1), 1374. https://doi.org/10.1038/s41467-022-28791-x.

(25) Pogna, E. A. A.; Viti, L.; Politano, A.; Brambilla, M.; Scamarcio, G.; Vitiello, M. S. Mapping Propagation of Collective Modes in Bi2Se3 and Bi2Te2.2Se0.8 Topological Insulators by near-Field Terahertz Nanoscopy. *Nat Commun* **2021**, *12* (1), 6672. https://doi.org/10.1038/s41467-021-26831-6.

(26) Wang, C.; Huang, S.; Xing, Q.; Xie, Y.; Song, C.; Wang, F.; Yan, H. Van Der Waals Thin Films of WTe2 for Natural Hyperbolic Plasmonic Surfaces. *Nat Commun* **2020**, *11* (1), 1158. https://doi.org/10.1038/s41467-020-15001-9.

(27) Nörenberg, T.; Álvarez-Pérez, G.; Obst, M.; Wehmeier, L.; Hempel, F.; Klopf, J. M.; Nikitin, A. Y.; Kehr, S. C.; Eng, L. M.; Alonso-González, P.; De Oliveira, T. V. A. G. Germanium Monosulfide as a Natural Platform for Highly Anisotropic THz Polaritons. *ACS Nano* **2022**, *16* (12), 20174–20185. https://doi.org/10.1021/acsnano.2c05376.

(28) Kowalski, R. A.; Nolen, J. R.; Varnavides, G.; Silva, S. M.; Allen, J. E.; Ciccarino, C. J.; Juraschek, D. M.; Law, S.; Narang, P.; Caldwell, J. D. Mid- to Far-Infrared Anisotropic

Dielectric Function of HfS 2 and HfSe 2. *Adv Opt Mater* **2022**, *10* (23), 2200933. https://doi.org/10.1002/adom.202200933.

(29) Chaudhary, K.; Tamagnone, M.; Yin, X.; Spägele, C. M.; Oscurato, S. L.; Li, J.; Persch, C.; Li, R.; Rubin, N. A.; Jauregui, L. A.; Watanabe, K.; Taniguchi, T.; Kim, P.; Wuttig, M.; Edgar, J. H.; Ambrosio, A.; Capasso, F. Polariton Nanophotonics Using Phase-Change Materials. *Nat Commun* **2019**, *10* (1), 4487. https://doi.org/10.1038/s41467-019-12439-4.

(30) Dolado, I.; Alfaro-Mozaz, F. J.; Li, P.; Nikulina, E.; Bylinkin, A.; Liu, S.; Edgar, J. H.; Casanova, F.; Hueso, L. E.; Alonso-González, P.; Vélez, S.; Nikitin, A. Y.; Hillenbrand, R. Nanoscale Guiding of Infrared Light with Hyperbolic Volume and Surface Polaritons in van Der Waals Material Ribbons. *Advanced Materials* **2020**, *32* (9), 1906530. https://doi.org/10.1002/adma.201906530.

(31) Barcelos, I. D.; Canassa, T. A.; Mayer, R. A.; Feres, F. H.; de Oliveira, E. G.; Goncalves, A.-M. B.; Bechtel, H. A.; Freitas, R. O.; Maia, F. C. B.; Alves, D. C. B. Ultrabroadband Nanocavity of Hyperbolic Phonon–Polaritons in 1D-Like α-MoO3. *ACS Photonics* **2021**, *8* (10), 3017–3026. https://doi.org/10.1021/acsphotonics.1c00955.

(32) Feres, F. H.; Mayer, R. A.; Wehmeier, L.; Maia, F. C. B.; Viana, E. R.; Malachias, A.; Bechtel, H. A.; Klopf, J. M.; Eng, L. M.; Kehr, S. C.; González, J. C.; Freitas, R. O.; Barcelos, I. D. Sub-Diffractional Cavity Modes of Terahertz Hyperbolic Phonon Polaritons in Tin Oxide. *Nat Commun* **2021**, *12* (1), 1–9. https://doi.org/10.1038/s41467-021-22209-w.

(33) Shi, Z.; Hong, X.; Bechtel, H. A.; Zeng, B.; Martin, M. C.; Watanabe, K.; Taniguchi, T.; Shen, Y.-R.; Wang, F. Observation of a Luttinger-Liquid Plasmon in Metallic Single-Walled Carbon Nanotubes. *Nat Photonics* **2015**, *9* (8), 515–519. https://doi.org/10.1038/nphoton.2015.123.

(34) Phillips, C.; Gilburd, L.; Xu, X. G.; Walker, G. C. Surface and Volume Phonon Polaritons in Boron Nitride Nanotubes. *J Phys Chem Lett* **2019**, *10* (17), 4851–4856. https://doi.org/10.1021/acs.jpclett.9b01829.

(35) Alfaro-Mozaz, F. J.; Alonso-González, P.; Vélez, S.; Dolado, I.; Autore, M.; Mastel, S.; Casanova, F.; Hueso, L. E.; Li, P.; Nikitin, A. Y.; Hillenbrand, R. Nanoimaging of Resonating Hyperbolic Polaritons in Linear Boron Nitride Antennas. *Nat Commun* **2017**, *8* (1), 15624. https://doi.org/10.1038/ncomms15624.

(36) Sotome, M.; Kida, N.; Takeda, R.; Okamoto, H. Terahertz Radiation Induced by Coherent Phonon Generation via Impulsive Stimulated Raman Scattering in Paratellurite. *Phys Rev A (Coll Park)* **2014**, *90* (3), 033842. https://doi.org/10.1103/PhysRevA.90.033842.

(37) McAllister, L.; Daly, M.; Chandler, P.; -, al; Yek, X.; Dunham, M. M.; Arce, H. G. *Acoustooptical Light Deflector Using TeO 2 Single Crystal To Cite This Article: Naoya Uchida and Yoshiro Ohmachi*; 1970; Vol. 9.

(38) Antonov, S. N. Acousto-Optic Deflector Based on a Paratellurite Crystal Using Broadband Acoustic Adhesive Contact. *Acoust Phys* **2017**, *63* (4), 410–415. https://doi.org/10.1134/S1063771017030010.

(39) Komandin, G.; Nozdrin, V.; Chuchupal, S.; Lomonov, V.; Pisarevskii, Y.; Porodinkov, O.; Spektor, I. Assessment of the Application of Paratellurite for the Acousto-Optical Deflection of Terahertz Rays Based on Broadband Spectroscopy Data. *J Phys D Appl Phys* **2020**, *53* (49), 495102. https://doi.org/10.1088/1361-6463/abafdc.

(40) Chemla, D. S.; Jerphagnon, J. Optical Second-Harmonic Generation in Paratellurite and Kleinman's Symmetry Relations. *Appl Phys Lett* **1972**, *20* (6), 222–223. https://doi.org/10.1063/1.1654119.

(41) Duclère, J.-R.; Hayakawa, T.; Roginskii, E. M.; Smirnov, M. B.; Mirgorodsky, A.; Couderc, V.; Masson, O.; Colas, M.; Noguera, O.; Rodriguez, V.; Thomas, P. Third Order Nonlinear Optical Properties of a Paratellurite Single Crystal. *J Appl Phys* **2018**, *123* (18), 183105. https://doi.org/10.1063/1.5020646.

(42) Liu, Z.; Yamazaki, T.; Shen, Y.; Kikuta, T.; Nakatani, N. Synthesis and Characterization of TeO2 Nanowires. *Jpn J Appl Phys* **2008**, *47* (1 PART 2), 771–774. https://doi.org/10.1143/JJAP.47.771.

(43) Siciliano, T.; Tepore, A.; Micocci, G.; Genga, A.; Siciliano, M.; Filippo, E. Transition from N- to p-Type Electrical Conductivity Induced by Ethanol Adsorption on α-Tellurium Dioxide Nanowires. *Sens Actuators B Chem* **2009**, *138* (1), 207–213. https://doi.org/https://doi.org/10.1016/j.snb.2009.02.007.

(44) Yan, C.; Huy Le, B.; Kang, D. J. Ultrasensitive Single Crystalline TeO2 Nanowire Based Hydrogen Gas Sensors. *J Mater Chem A Mater* **2014**, *2* (15), 5394–5398. https://doi.org/10.1039/c4ta00135d.

(45) Noguera, O.; Merle-Méjean, T.; Mirgorodsky, A. P.; Smirnov, M. B.; Thomas, P.; Champarnaud-Mesjard, J. C. Vibrational and Structural Properties of Glass and Crystalline Phases of TeO2. *J Non Cryst Solids* **2003**, *330* (1–3), 50–60. https://doi.org/10.1016/j.jnoncrysol.2003.08.052.

(46) Mirgorodsky, A. P.; Merle-Méjean, T.; Champarnaud, J.-C.; Thomas, P.; Frit, B. Dynamics and Structure of TeO2 Polymorphs: Model Treatment of Paratellurite and Tellurite; Raman Scattering Evidence for New γ- and δ-Phases. *Journal of Physics and Chemistry of Solids* **2000**, *61* (4), 501–509. https://doi.org/https://doi.org/10.1016/S0022-3697(99)00263-2.

(47) Korn, D. M.; Pine, A. S.; Dresselhaus, G.; Reed, T. B. Infrared Reflectivity of Paratellurite, TeO2. *Phys Rev B* **1973**, *8* (2), 768–772. https://doi.org/10.1103/PhysRevB.8.768.

(48) Dai, S.; Fei, Z.; Ma, Q.; Rodin, A. S.; Wagner, M.; McLeod, A. S.; Liu, M. K.; Gannett, W.; Regan, W.; Watanabe, K.; Taniguchi, T.; Thiemens, M.; Dominguez, G.; Neto, A. H.

C.; Zettl, A.; Keilmann, F.; Jarillo-Herrero, P.; Fogler, M. M.; Basov, D. N. Tunable Phonon Polaritons in Atomically Thin van Der Waals Crystals of Boron Nitride. *Science (1979)* **2014**, *343* (6175), 1125–1129. https://doi.org/10.1126/science.1246833.

(49) Li, J.; Gan, R.; Guo, Q.; Liu, H.; Xu, J.; Yi, F. Tailoring Optical Responses of Infrared Plasmonic Metamaterial Absorbers by Optical Phonons. *Opt Express* **2018**, *26* (13), 16769–16781. https://doi.org/10.1364/OE.26.016769.

(50) Luxmoore, I. J.; Gan, C. H.; Liu, P. Q.; Valmorra, F.; Li, P.; Faist, J.; Nash, G. R. Strong Coupling in the Far-Infrared between Graphene Plasmons and the Surface Optical Phonons of Silicon Dioxide. *ACS Photonics* **2014**, *1* (11), 1151–1155. https://doi.org/10.1021/ph500233s.

(51) Solymar, L.; Shamonina, E. *Waves in Metamaterials*; Oxford University PressOxford, 2009. https://doi.org/10.1093/oso/9780199215331.001.0001.

(52) Schwartz, J. J.; Le, S. T.; Krylyuk, S.; Richter, C. A.; Davydov, A. V; Centrone, A. Substrate-Mediated Hyperbolic Phonon Polaritons in MoO3. *Nanophotonics* **2021**, *10* (5), 1517–1527. https://doi.org/doi:10.1515/nanoph-2020-0640.

(53) Feres, F. H.; Mayer, R. A.; Barcelos, I. D.; Freitas, R. O.; Maia, F. C. B. Acceleration of Subwavelength Polaritons by Engineering Dielectric-Metallic Substrates. *ACS Photonics* **2020**, *7* (6), 1396–1402. https://doi.org/10.1021/acsphotonics.0c00563.

(54) Hermann, P.; Hoehl, A.; Patoka, P.; Huth, F.; Rühl, E.; Ulm, G. Near-Field Imaging and Nano-Fourier-Transform Infrared Spectroscopy Using Broadband Synchrotron Radiation. *Opt Express* **2013**, *21* (3), 2913. https://doi.org/10.1364/OE.21.002913.

(55) Bechtel, H. A.; Muller, E. A.; Olmon, R. L.; Martin, M. C.; Raschke, M. B. Ultrabroadband Infrared Nanospectroscopic Imaging. *Proceedings of the National Academy of Sciences* **2014**, *111* (20), 7191–7196. https://doi.org/10.1073/pnas.1400502111.

(56) Freitas, R. O.; Deneke, C.; Maia, F. C. B.; Medeiros, H. G.; Moreno, T.; Dumas, P.; Petroff, Y.; Westfahl, H. Low-Aberration Beamline Optics for Synchrotron Infrared Nanospectroscopy. *Opt Express* **2018**, *26* (9), 11238. https://doi.org/10.1364/oe.26.011238.

(57) Barcelos, I. D.; Bechtel, H. A.; de Matos, C. J. S.; Bahamon, D. A.; Kaestner, B.; Maia, F. C. B.; Freitas, R. O. Probing Polaritons in 2D Materials with Synchrotron Infrared Nanospectroscopy. *Adv Opt Mater* **2020**, *8* (5), 1–16. https://doi.org/10.1002/adom.201901091.

(58) McLeod, A. S.; Kelly, P.; Goldflam, M. D.; Gainsforth, Z.; Westphal, A. J.; Dominguez, G.; Thiemens, M. H.; Fogler, M. M.; Basov, D. N. Model for Quantitative Tip-Enhanced Spectroscopy and the Extraction of Nanoscale-Resolved Optical Constants. *Phys Rev B* **2014**, *90* (8), 085136. https://doi.org/10.1103/PhysRevB.90.085136.

(59) Knoll, B.; Keilmann, F. Near-Field Probing of Vibrational Absorption for Chemical Microscopy. *Nature* **1999**, *399* (6732), 134–137. https://doi.org/10.1038/20154.

(60) Zenhausern, F.; Martin, Y.; Wickramasinghe, H. K. Scanning Interferometric Apertureless Microscopy: Optical Imaging at 10 Angstrom Resolution. *Science (1979)* **1995**, *269* (5227), 1083–1085. https://doi.org/10.1126/science.269.5227.1083.

(61) Chen, X.; Yao, Z.; Stanciu, S. G.; Basov, D. N.; Hillenbrand, R.; Liu, M. Rapid Simulations of Hyperspectral Near-Field Images of Three-Dimensional Heterogeneous Surfaces. *Opt Express* **2021**, *29* (24), 39648–39668. https://doi.org/10.1364/OE.440821.

(62) Obst, M.; Nörenberg, T.; Álvarez-Pérez, G.; de Oliveira, T. V. A. G.; Taboada-Gutiérrez, J.; Feres, F. H.; Kaps, F. G.; Hatem, O.; Luferau, A.; Nikitin, A. Y.; Klopf, J. M.; Alonso-González, P.; Kehr, S. C.; Eng, L. M. Terahertz Twistoptics–Engineering Canalized Phonon Polaritons. *ACS Nano* **2023**, *17* (19), 19313–19322. https://doi.org/10.1021/acsnano.3c06477.

(63) Dolado, I.; Alfaro-Mozaz, F. J.; Li, P.; Nikulina, E.; Bylinkin, A.; Liu, S.; Edgar, J. H.; Casanova, F.; Hueso, L. E.; Alonso-González, P.; Vélez, S.; Nikitin, A. Y.; Hillenbrand, R. Nanoscale Guiding of Infrared Light with Hyperbolic Volume and Surface Polaritons in van Der Waals Material Ribbons. *Advanced Materials* **2020**, *32* (9), 1906530. https://doi.org/10.1002/adma.201906530.

(64) Chen, S.; Bylinkin, A.; Wang, Z.; Schnell, M.; Chandan, G.; Li, P.; Nikitin, A. Y.; Law, S.; Hillenbrand, R. Real-Space Nanoimaging of THz Polaritons in the Topological Insulator Bi2Se3. *Nat Commun* **2022**, *13* (1), 1374. https://doi.org/10.1038/s41467-022-28791-x.

(65) Hu, G.; Ou, Q.; Si, G.; Wu, Y.; Wu, J.; Dai, Z.; Krasnok, A.; Mazor, Y.; Zhang, Q.; Bao, Q.; Qiu, C. W.; Alù, A. Topological Polaritons and Photonic Magic Angles in Twisted α-MoO3 Bilayers. *Nature* **2020**, *582* (7811), 209–213. https://doi.org/10.1038/s41586-020-2359-9.

(66) Duan, J.; Álvarez-Pérez, G.; Lanza, C.; Voronin, K.; Tresguerres-Mata, A. I. F.; Capote-Robayna, N.; Álvarez-Cuervo, J.; Tarazaga Martín-Luengo, A.; Martín-Sánchez, J.; Volkov, V. S.; Nikitin, A. Y.; Alonso-González, P. Multiple and Spectrally Robust Photonic Magic Angles in Reconfigurable α-MoO3 Trilayers. *Nat Mater* **2023**, *22* (7), 867–872. https://doi.org/10.1038/s41563-023-01582-5.

(67) Alfaro-Mozaz, F. J.; Alonso-González, P.; Vélez, S.; Dolado, I.; Autore, M.; Mastel, S.; Casanova, F.; Hueso, L. E.; Li, P.; Nikitin, A. Y.; Hillenbrand, R.; Hillenbrand, & R. Nanoimaging of Resonating Hyperbolic Polaritons in Linear Boron Nitride Antennas. *Nat Commun* **2017**, *8*, 15624. https://doi.org/10.1038/ncomms15624.

(68) Wehmeier, L.; Lang, D.; Liu, Y.; Zhang, X.; Winnerl, S.; Eng, L. M.; Kehr, S. C. Polarization-Dependent near-Field Phonon Nanoscopy of Oxides: SrTiO3 , LiNbO3 , and

PbZr0.2Ti0.8O3. *Phys Rev B* **2019**, *100* (3), 035444. https://doi.org/10.1103/PhysRevB.100.035444.

(69) Cuisset, A.; Hindle, F.; Mouret, G.; Bocquet, R.; Bruckhuisen, J.; Decker, J.; Pienkina, A.; Bray, C.; Fertein, É.; Boudon, V. Terahertz Rotational Spectroscopy of Greenhouse Gases Using Long Interaction Path-Lengths. *Applied Sciences* **2021**, *11* (3), 1229. https://doi.org/10.3390/app11031229.

(70) Abina, A.; Puc, U.; Jazbinšek, M.; Zidanšek, A. Analytical Gas Sensing in the Terahertz Spectral Range. *Micromachines (Basel)* **2023**, *14* (11), 1987. https://doi.org/10.3390/mi14111987.

(71) Razdolski, I.; Chen, Y.; Giles, A. J.; Gewinner, S.; Schöllkopf, W.; Hong, M.; Wolf, M.; Giannini, V.; Caldwell, J. D.; Maier, S. A.; Paarmann, A. Resonant Enhancement of Second-Harmonic Generation in the Mid-Infrared Using Localized Surface Phonon Polaritons in Subdiffractional Nanostructures. *Nano Lett* **2016**, *16* (11), 6954–6959. https://doi.org/10.1021/acs.nanolett.6b03014.

(72) Bechtel, H. A.; Johnson, S. C.; Khatib, O.; Muller, E. A.; Raschke, M. B. Synchrotron Infrared Nano-Spectroscopy and -Imaging. *Surf Sci Rep* **2020**, *75* (3), 100493. https://doi.org/10.1016/j.surfrep.2020.100493.

(73) Dapolito, M.; Tsuneto, M.; Zheng, W.; Wehmeier, L.; Xu, S.; Chen, X.; Sun, J.; Du, Z.; Shao, Y.; Jing, R.; Zhang, S.; Bercher, A.; Dong, Y.; Halbertal, D.; Ravindran, V.; Zhou, Z.; Petrovic, M.; Gozar, A.; Carr, G. L.; Li, Q.; Kuzmenko, A. B.; Fogler, M. M.; Basov, D. N.; Du, X.; Liu, M. Infrared Nano-Imaging of Dirac Magnetoexcitons in Graphene. *Nat Nanotechnol* **2023**, *18* (12), 1409–1415. https://doi.org/10.1038/s41565-023-01488-y.